Supplementary Information for

Electrically Controlled Spatial Light Modulator for Ultrawideband Hyperspectral Terahertz Single-Pixel Imaging

Xudong Liu[1], Wenjing Ma[2], Chenyu Wang[3], Chuanfu Sun[3], Yu Liao[3], Emma Pickwell-MacPherson[4], Xiaoyu Weng[1]¶, Junle Qu[1]#, Songlin Zhuang[5] & Yiwen Sun[1]*

[1]Key Laboratory of Optoelectronic Devices and Systems of Ministry of Education and Guangdong Province, College of Physics and Optoelectronics Engineering, Shenzhen University, Shenzhen, 518060, China

[2]National Engineering Laboratory for Big Data System Computing Technology, Shenzhen University, Shenzhen 518060, China

[3]Department of Biomedical Engineering, School of Medicine, Shenzhen University, Shenzhen 518060, China

[4]Department of Physics, University of Warwick, Coventry CV4 7AL, United Kingdom

[5]School of Optical-Electrical and Computer Engineering, University of Shanghai for Science and Technology, Shanghai, China

¶xiaoyu@szu.edu.cn, #jlqu@szu.edu.cn, *ywsun@szu.edu.cn

Supplementary Note 1. Structure details of the terahertz spatial light modulator (THz-SLM)

This device comprises a planar array of subwavelength microslit elements fabricated on epitaxial *n*-doped GaAs, grown on a semi-insulating GaAs substrate. Each pixel of the terahertz SLM consists of a 3×3 mm^2 area with 375 grating periods, as illustrated in Fig. S1. The microslit elements feature a 200-nm-thick gold layer, a 6 μm width, and a 2 μm gap spacing. These elements are connected via a contact pad, functioning as a metallic Schottky gate. An external voltage bias modulates the charge carrier density in the substrate near the microslit gaps, enabling tunable absorption of terahertz waves. The THz SLM is configured as a 10×10 array, with each pixel independently controlled by an external voltage applied between the Schottky contact and the Ohmic contact.

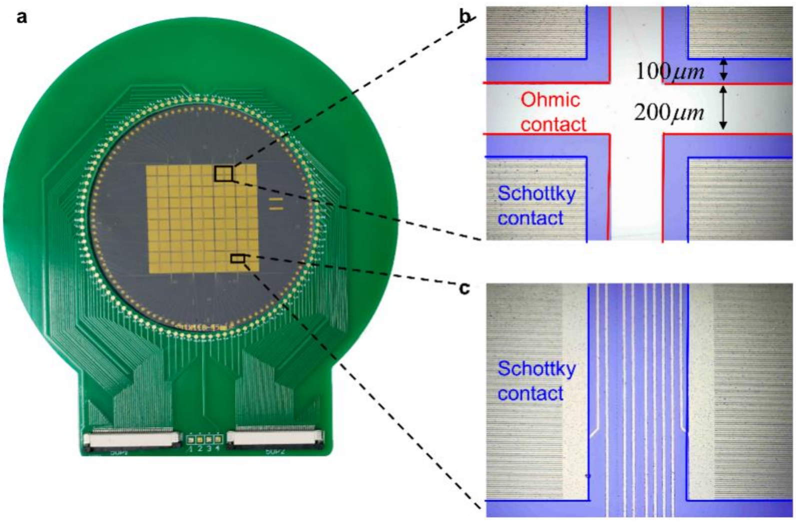

Fig. S1 Photograph and microscopy image of the fabricated THz-SLM. Each pixel contains gold microslits functioning as Schottky contacts. These microslits were individually connected to an external voltage source, enabling independent pixel control. Gold stripes, acting as Ohmic contacts, are positioned between the pixels and share a common 5 V electrode.

Supplementary Note 2. Voltage control circuit board

The MCU delivers control signals to the shifter register (74LVX595) via GPIO ports. These signals drive the 100 MOSFETs and corresponding LEDs, with the LEDs providing real-time visual feedback on the pixel switching status for monitoring spatial encoding patterns of the THz-SLM. The MOSFET outputs are routed through two 50-pin FPC connectors, which interface with the THz-SLM adapter board via FPC cables to regulate individual pixel states.

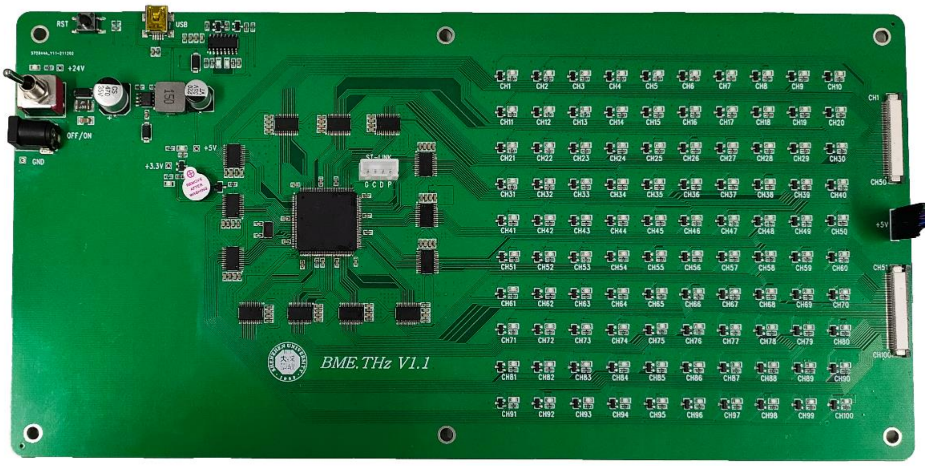

Fig. S2 Photograph of the custom voltage-control circuit board for electrical addressing of the THz-SLM. The board integrates the MCU, shift-register control modules, MOSFET switching channels, status-indicator LEDs, and FPC interfaces required for independent addressing of the 10×10 THz-SLM pixels. The LED array provides visual confirmation of the loaded binary mask patterns during spatial encoding.

Supplementary Note 3. Operational frequency of the THz-SLM

The modulation speed of the THz-SLM depends on the conductivity variation frequency in the *n*-GaAs layer. This parameter can be indirectly characterized by measuring terahertz wave transmittance changes under square-wave voltage excitation at different frequencies. Fig. S3a and S3b illustrate the experimental setup for speed measurement. In the experiment, the optical delay line was fixed at the time-domain signal peak position (corresponding to the maximum terahertz pulse electric field) to optimize detection signal-to-noise ratio. A control circuit generated square-wave driving signals (0-5 V amplitude, 50% duty cycle) with frequencies ranging from 1 Hz to 20 kHz, synchronously switching all THz-SLM pixels. The terahertz detector output was recorded using an oscilloscope (Tektronix TBS 1072B) configured in rising-edge trigger mode to ensure precise synchronization with the driving signal. At each driving frequency, the oscilloscope-captured output voltage waveforms were recorded. The raw experimental data corresponding to the fitted results in Figure 2f are presented in Fig. S3c-S3f.

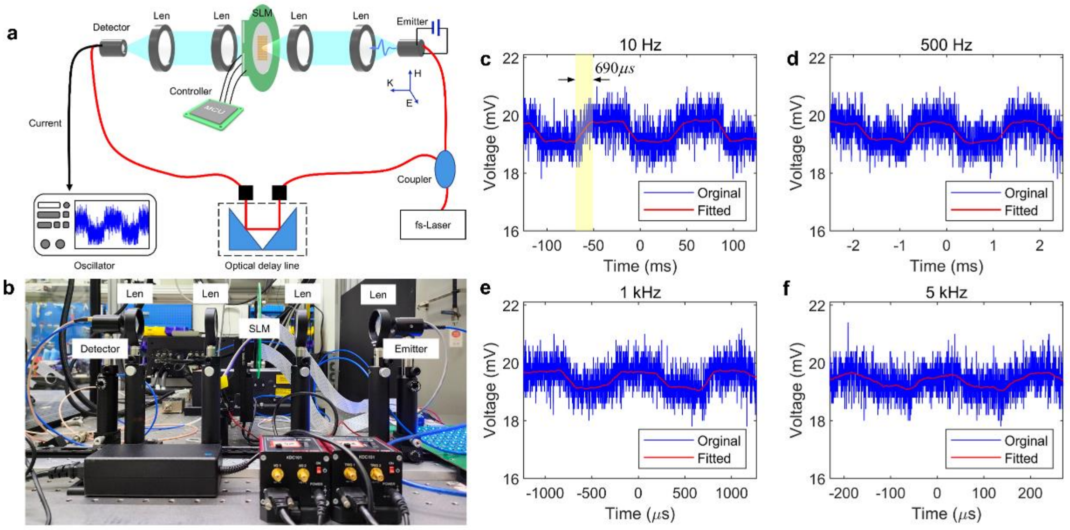

Fig. S3 Modulation speed measurement and fitting. a and **b** are schematic and experimental setup of the modulation speed measurement system. **c-f** are modulated terahertz beam signals under 0-5 V square-wave driving at 10 Hz, 500 Hz, 1 kHz and 5 kHz, with red curves showing the fitted results.

Supplementary Note 4. Frequency-dependent modulation-depth maps of the THz-SLM from 0.2 to 1.4 THz

To further characterize the spatial uniformity and frequency-dependent response of the electrically controlled THz-SLM, modulation-depth maps were extracted at representative frequencies from 0.2 to 1.4 THz. These maps were obtained from the focused-beam raster-scan measurement used for the spatial modulation characterization in Figure 2g of the main text. At each scanned position, the THz waveforms measured under 0 V and 5 V reverse-bias states were Fourier transformed, and the corresponding frequency-domain field amplitudes were extracted.

The modulation depth was defined as an intensity-domain quantity: $MD(x, y, f) = [1 - |E_{0V}(x, y, f)|^2/|E_{5V}(x, y, f)|^2] \times 100\%$, where $E_{0V}(x, y, f)$ and $E_{5V}(x, y, f)$ are the Fourier-domain THz field amplitudes measured at position (x, y) under 0 V and 5 V reverse bias, respectively. In this device, the 0 V state corresponds to the low-transmission state because of free-carrier absorption in the *n*-GaAs layer, whereas the 5 V reverse-biased state corresponds to the high-transmission state due to carrier depletion beneath the Schottky microslits. Therefore, the squared field amplitudes were used to evaluate the relative intensity modulation between the two bias states.

As shown in Fig. S4, the THz-SLM exhibits a spatially addressable, pixelated modulation response over the measured active area across the 0.2–1.4 THz range. The modulation depth shows a frequency-dependent behavior. The relatively low modulation depth near 0.2 THz is mainly caused by the reduced signal-to-noise ratio of the THz-TDS system below 0.3 THz. In contrast, the decrease in modulation depth above approximately 1.2 THz is mainly attributed to the Drude-type free-carrier response of n-GaAs, where the real part of the conductivity and the corresponding absorption contrast decrease at higher frequencies. Thus, the observed modulation-depth distribution is governed by both the usable spectral window of the THz-TDS system and the intrinsic carrier-response characteristics of the GaAs Schottky microslit device, consistent with the broadband modulation spectrum measured from a representative pixel in Figure 2e of the main text. The black dashed square indicates the 8×8 subarray selected for the imaging experiments, while the red crosses mark the three non-functional pixels excluded from the imaging region.

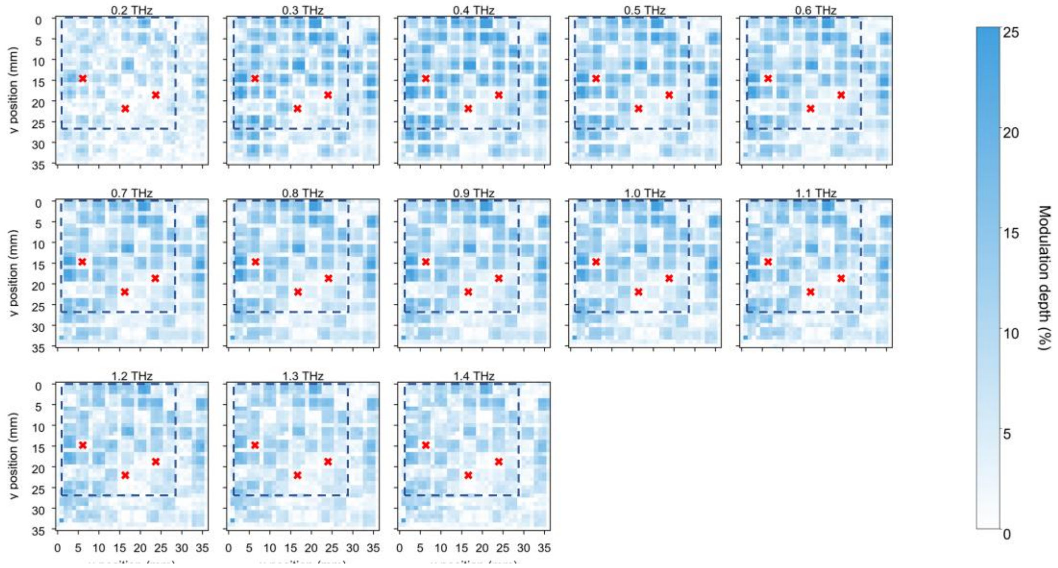

Fig. S4 Frequency-dependent modulation-depth maps of the THz-SLM from 0.2 to 1.4 THz. The modulation-depth maps were extracted from focused-beam raster-scan measurements at representative frequencies from 0.2 to 1.4 THz. The modulation depth was calculated from the squared Fourier-domain field amplitudes measured under 0 V and 5 V reverse bias. All maps are displayed using the same color scale from 0% to 25% to allow direct comparison of the spatial modulation response at different frequencies. The THz-SLM exhibits a spatially addressable pixelated modulation response over the measured active area. The black dashed square indicates the 8×8 subarray selected for the imaging experiments, while the red crosses mark the three non-functional pixels excluded from the imaging region.

Supplementary Note 5. Ordering of Hadamard basis patterns using the Diag strategy

To improve reconstruction robustness under practical THz imaging conditions, we developed a Diag-ordered Hadamard sampling strategy. After pixelation, the object is represented by a vector $X \in \Re^{N\times 1}$, N is the number of spatial pixels. The i-th single-pixel measurement is written as $y_i=\Phi_i X+\varepsilon_i$, where $\Phi_i \in \Re^{1\times N}$ denotes the spatial encoding pattern and ε_i represents measurement noise. After M measurements, the acquisition model becomes $Y=\Phi X+\varepsilon$, where $Y \in \Re^{M\times 1}$, $\Phi \in \Re^{M\times N}$, $\varepsilon \in \Re^{M\times 1}$. When $M<N$, the inverse problem is underdetermined and requires regularized reconstruction. In this work, the image was recovered using the augmented Lagrangian and alternating

direction algorithm (TVAL3), which exploits gradient sparsity through total-variation minimization.

Hadamard matrices are well suited to single-pixel imaging because their orthogonal binary patterns provide high throughput and favorable multiplexing efficiency. Since the present THz-SLM supports binary transmission states of 0 and 1, each ±1 Hadamard basis was implemented using a binary pattern and its complementary inverse. The difference between the two measured signals suppresses the background term and common-mode fluctuations, yielding one effective Hadamard coefficient. Therefore, acquisition of M coefficients requires $2M$ displayed binary masks.

The ordering of these coefficients is critical under undersampling and noise. For natural and piecewise-smooth images, most of the energy in the two-dimensional Walsh–Hadamard domain is concentrated in the low-sequency region, whereas high-sequency coefficients associated with edges and fine details generally have lower amplitudes and are more susceptible to noise. Here, sequency denotes the number of sign changes in a Hadamard basis pattern. Consequently, prioritizing low-sequency coefficients can improve reconstruction quality when only a subset of measurements is available.

The principle of the proposed Diag strategy is illustrated in Figure 3 of the main text. The corresponding spatial Hadamard patterns are generated directly from the sequency-domain coordinates. For each position along the Diag path, a two-dimensional unit impulse is placed at the selected sequency coordinate, and an inverse Walsh–Hadamard transform is applied to obtain the associated spatial basis pattern. Repeating this procedure produces the complete Diag-ordered sequence. The detailed generation procedures are summarized in Tables S1 and S2.

Compared with more complex sorting approaches such as Cake-Cutting, Diag follows a simple deterministic rule and does not require prior knowledge of the target.

This simplicity makes the pattern sequence easy to generate and computationally scalable. At the 4096×4096 scale, the ordering-generation time is reduced by approximately 99.4% relative to Cake-Cutting, as summarized in Table S3.

To verify the low-sequency energy concentration underlying the Diag strategy, eight standard grayscale images were resized to 64×64 pixels, as shown in Fig. S5. Their two-dimensional Walsh–Hadamard spectra in Fig. S6 exhibit strong energy concentration near the upper-left low-sequency region. Fig. S7 further compares the measurement distributions obtained with Natural, Walsh, Paley, Cake-Cutting, and Diag orderings. Both Cake-Cutting and Diag concentrate dominant coefficients near the beginning of the sequence, whereas Diag achieves this front-loaded acquisition through a direct deterministic traversal.

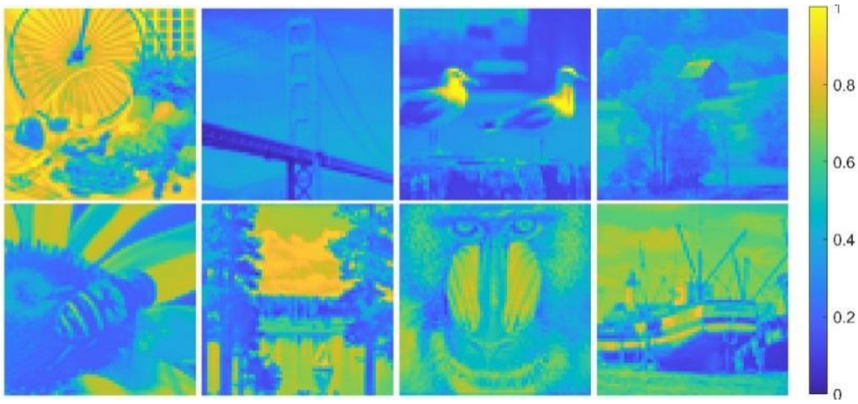

Fig. S5 Standard grayscale test images used for evaluating the robustness of Hadamard ordering strategies. All the images were resized to 64×64. The colormap is parula.

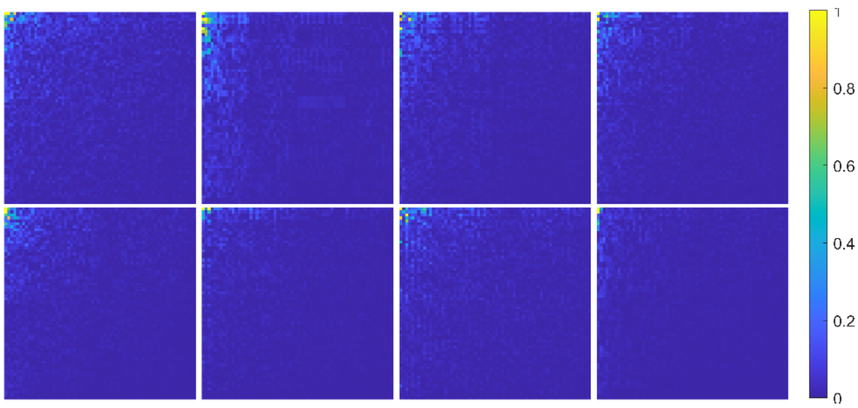

Fig. S6 Energy distribution of the test images in the two-dimensional Walsh–Hadamard domain. The spectra show strong energy concentration in the upper-left low-sequency region, confirming that low-sequency Hadamard coefficients carry most of the dominant image information.

Table. S1 Pseudo-code for Hadamard matrix construction based on diagonal scanning.

Algorithm 1: Direct Hadamard generation based on diag scanning order

Input: Image resolution N (N is a power of 2)

Output: Hadamard basis pattern sequence {H_k(x,y)} generated in Diag order

```
// Step 1: Generate coordinate sequence for Diag scanning path
scan_order = generate_Diag_order(N)
// Step 2: Directly generate basis patterns in Diag order
base_patterns = [ ]
for each (i, j) in scan_order do
    // Generate the unit impulse function δ_ij
    δ = zeros(N,N)        // Initialize an N×N matrix
    δ[i, j] = 1        // Set impulse at position (i,j)
    // Perform inverse Walsh-Hadamard transform to generate basis pattern
    H_k = inverse_walsh_Hadamard(δ)
    base_patterns.append(H_k)        // Store in Diag order
end for
return base_patterns
```

Table. S2 Pseudo-code for diagonal scanning path generation.

Algorithm 2: Function generate_Diag_order(N):

Input: Image resolution N (N is a power of 2)

Output: Scanning path coordinate sequence {scan_order} = [(i, j)]

```
scan_order = [ ];
for d = 1 to 2*N-1:
    if d <= N:
        start_i, start_j = 1, d
    else:
        start_i, start_j = d-N+1, N
    i, j = start_i, start_j
    while i <= N and j >= 1:
        scan_order.append((i, j))
```

```
            i += 1
            j -= 1
    return scan_order
```

Table. S3 Computational efficiency comparison between the Cake-Cutting (CC) and Diagonal (Diag) strategies for Hadamard pattern ordering.

Matrix size	CC strategy	Diag strategy
16×16	0.001 s	0.001 s
64×64	0.007 s	0.003 s
256×256	0.1 s	0.004 s
1024×1024	2.2 s	0.05 s
4096×4096	84.2 s	0.47 s

Note: The Diag strategy reduces runtime by over two orders of magnitude at the 4096×4096 scale, demonstrating superior scalability and efficiency for large-scale compressive imaging. The timing was measured on Intel i5-7300HQ CPU @ 2.50 GHz using MATLAB R2023a.

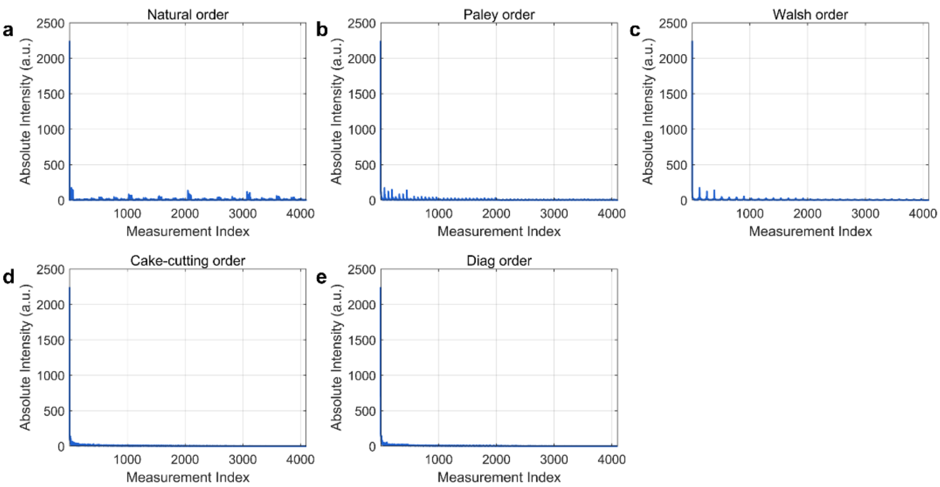

Fig. S7 Comparison of measurement-sequence distributions under different Hadamard ordering strategies. a. Natural ordering; **b.** Paley ordering; **c.** Walsh ordering; **d.** Cake-cutting ordering; **e.** Diag ordering. The plotted values represent the averaged absolute measurement coefficients obtained from the eight standard test images.

Since peak signal-to-noise ratio (PSNR) serves as a key metric for assessing reconstructed image quality in CS imaging, we calculated it using the following expression:

$$PSNR = 10 \times \log_{10}\left(\frac{\left(2^{m}-1\right)^{2}}{MSE}\right), \tag{1}$$

where m represents the bit-width of the pixel, the MSE represents the mean square error between reconstructed and actual imaging object data, which can be expressed as:

$$MSE = \frac{1}{n}\sum_{j=1}^{n}\left\| x_j - y_j \right\|^2 , \tag{2}$$

where n represents the number of pixels of the image, x_j denotes the pixel value of the original object image, and y_j represents the pixel value of the corresponding reconstructed image. The PSNR is a metric of similarity, the smaller the MSE, the larger the PSNR value, indicating higher image similarity.

Fig. S8–S10 show the reconstruction results under noiseless, 0 dB noise, and -10 dB noise conditions, respectively. Under noiseless and 0 dB noise conditions, all ordering strategies generally show improved PSNR as the sampling ratio increases, because more high-sequency details are included. Under strong noise conditions, however, acquiring additional high-sequency measurements can also introduce more noise-dominated coefficients. In this case, front-loaded strategies such as Cake-Cutting and Diag are advantageous at low sampling ratios because they prioritize high-energy, low-sequency measurements before noise accumulation becomes dominant. These results support the use of Diag ordering for THz single-pixel imaging, where the post-sample signal-to-noise ratio can be limited and the number of displayed masks must be minimized.

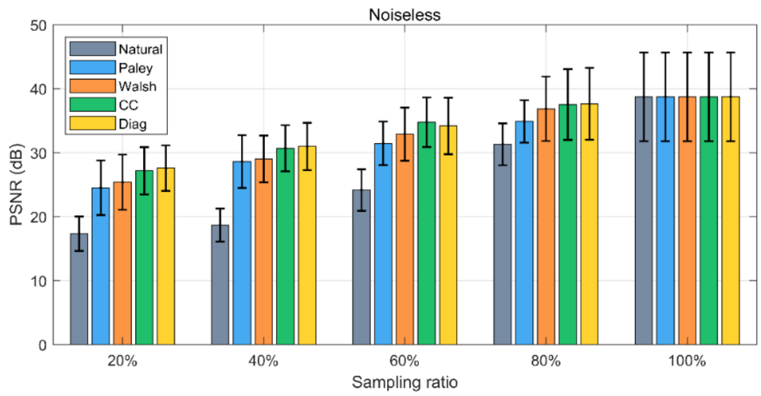

Fig. S8 Quantitative reconstruction performance using different Hadamard ordering strategies under noiseless conditions. PSNR values are compared at different sampling ratios.

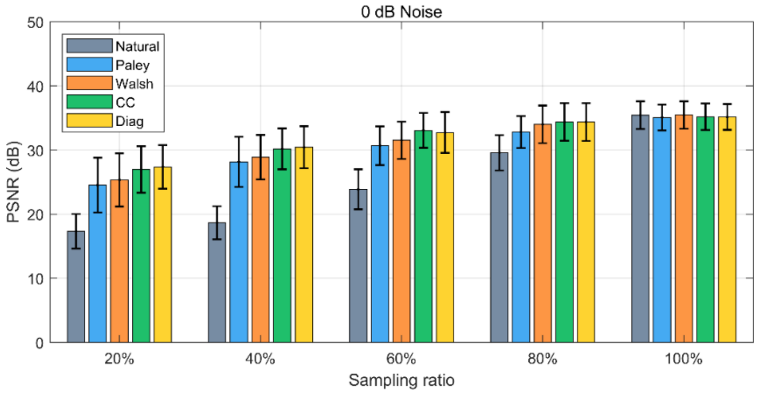

Fig. S9 Quantitative reconstruction performance using different Hadamard ordering strategies under 0 dB noise conditions. PSNR values are compared at different sampling ratios.

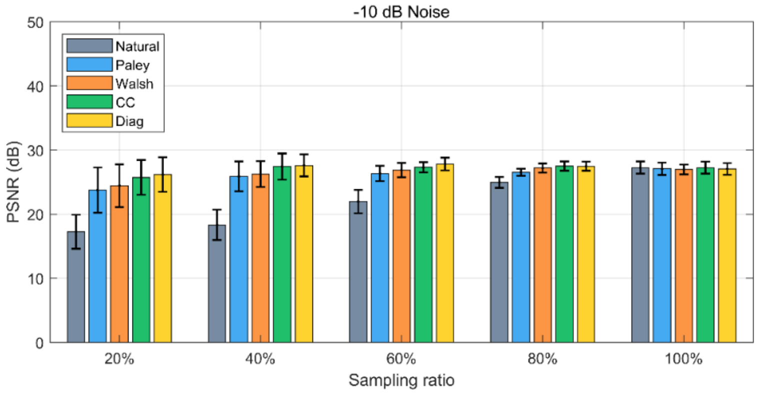

Fig. S10 Quantitative reconstruction performance using different Hadamard ordering strategies under -10 dB noise conditions. PSNR values are compared at different sampling ratios.

These results support the use of Diag as a balanced, deterministic, and computationally efficient Hadamard ordering strategy for THz compressed single-pixel imaging under low-SNR and undersampled conditions.

Supplementary Note 6. Image quality assessment (PSNR) from experimental data at varying sampling rates

To further evaluate the influence of Hadamard ordering on experimental THz single-pixel reconstruction, we calculated the PSNR of reconstructed images obtained with different ordering strategies at varying sampling ratios. The comparison was performed using the same experimentally acquired THz single-pixel measurement data, the same reconstruction algorithm, and the same reconstruction parameters. Therefore, the ordering strategy was the only variable in this analysis. Natural, Walsh, Paley, Cake-Cutting, and Diag orderings were compared at four representative frequencies: 0.25 THz, 0.45 THz, 0.65 THz, and 0.85 THz.

As shown in Fig. S11, the PSNR generally increases or remains stable as the sampling ratio increases, indicating that additional Hadamard coefficients improve the reconstruction fidelity by incorporating more spatial information. The Diag ordering provides consistently stable performance across the tested frequency range and sampling ratios. In particular, at relatively low sampling ratios, Diag generally yields higher or comparable PSNR compared with the conventional Natural, Walsh, and Paley orderings. Cake-Cutting also shows competitive reconstruction performance, especially at intermediate and high sampling ratios. These results indicate that front-loaded low-sequency ordering strategies are advantageous for experimental THz single-pixel imaging, where the measured signal is affected by limited modulation depth, illumination nonuniformity, and detector noise. Compared with Cake-Cutting, however, the Diag ordering can be generated through a simple deterministic diagonal traversal of the two-dimensional sequency domain, providing higher computational efficiency and faster pattern-sequence generation, as discussed in the main text.

The frequency-dependent PSNR variation reflects the combined influence of the THz-TDS spectral signal-to-noise ratio, the modulation response of the THz-SLM, and the sample-dependent transmitted signal strength. The PSNR values at 0.25 THz and 0.45 THz are generally higher than those at 0.65 THz and 0.85 THz, consistent with the stronger modulation response and higher usable signal level in the lower-frequency range. Nevertheless, all five ordering strategies allow image reconstruction at the four selected frequencies, confirming that frequency-resolved THz single-pixel imaging can be performed over the effective operating bandwidth of the system. The relatively stable PSNR of Diag across different frequencies supports its use as a practical Hadamard ordering strategy for electrically encoded THz single-pixel imaging.

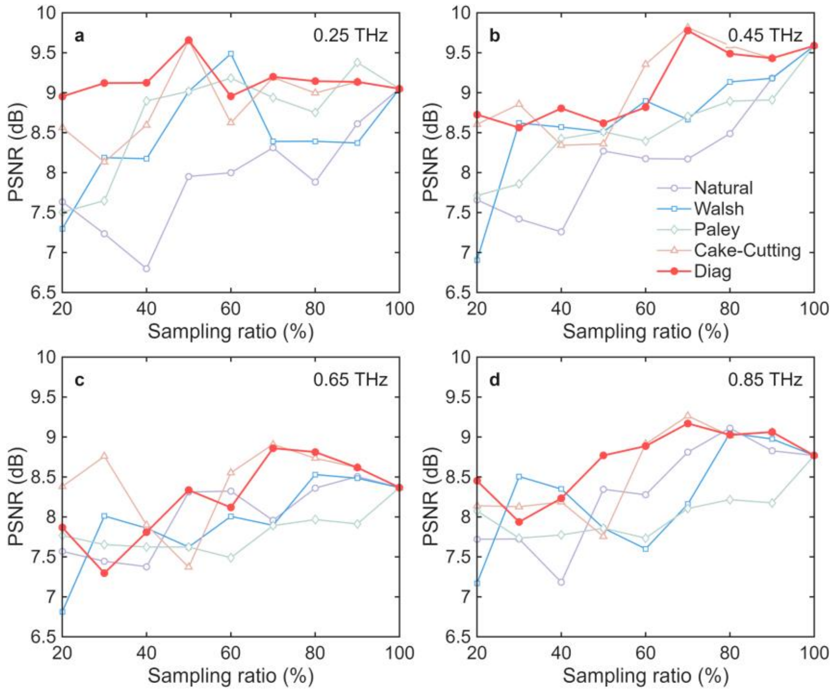

Fig. S11 Experimental PSNR comparison of different Hadamard ordering strategies for frequency-resolved THz single-pixel imaging. PSNR values of reconstructed metallic-aperture images were calculated at different sampling ratios using Natural, Walsh, Paley, Cake-Cutting, and Diag orderings. The comparison was performed at four representative frequencies: **a**, 0.25 THz; **b**, 0.45 THz; **c**, 0.65 THz; and **d**, 0.85 THz. All reconstructions were performed using the same experimentally acquired THz single-pixel measurement data and the same reconstruction parameters, so that the ordering strategy was the only variable. The Diag ordering shows stable reconstruction performance across different sampling ratios and frequencies, while Cake-Cutting also provides competitive performance at intermediate and high sampling ratios.

Supplementary Note 7. Normal-incidence reflection-mode THz single-pixel imaging system

A normal-incidence reflection-mode THz single-pixel imaging setup is shown in Fig. S12. The system consists of a THz emitter, focusing lenses, a silicon beam splitter, the electrically controlled THz-SLM, a reflective sample, and a single photoconductive detector. In this geometry, the incident THz beam is directed onto the sample by the beam splitter (BS), and the reflected THz field from the sample is subsequently encoded by the THz-SLM before being collected by the detector. The reflective sample was a metallic step structure with two regions of different thicknesses. The thick and thin metal regions had thicknesses of 2 mm and 1 mm, respectively, and each region occupied an area of 20 × 20 mm² within the imaging field of view. Reflections from the two metal surfaces produced different time-of-flight delays in the measured THz waveform. By extracting the single-pixel signals at selected temporal delays and reconstructing the corresponding spatial maps, the system enables reflection-mode depth-resolved THz single-pixel imaging.

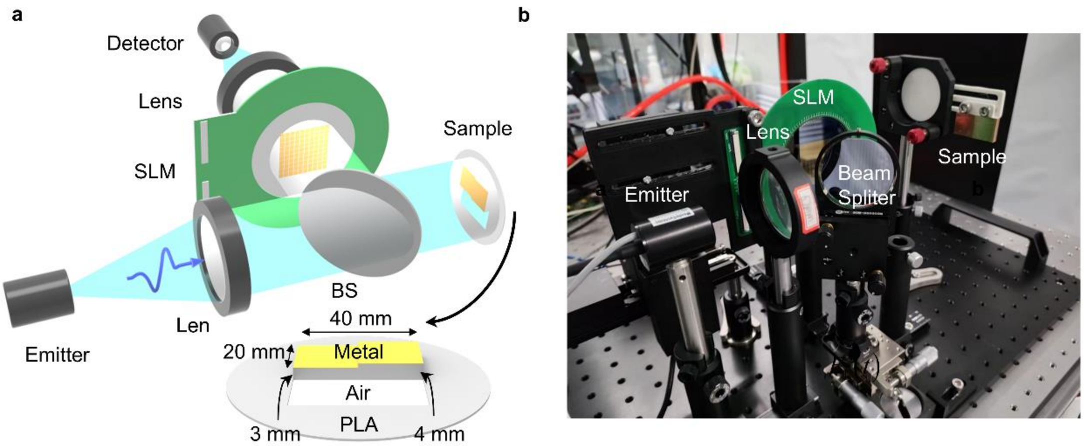

Fig. S12 Schematic and photograph of the normal-incidence reflection-mode THz single-pixel imaging setup. a. Schematic of the reflection-mode optical layout. The THz beam is directed to the metallic step sample by a silicon beam splitter, and the reflected THz field is spatially encoded by the THz-SLM before detection. **b**. Photograph of the experimental setup.

Supplementary Note 8. Role of the THz-SLM in transmission and reflection geometries

Although the physical placement of the THz-SLM differs between the transmission and reflection configurations, its algorithmic role in the single-pixel imaging process is the same. In both cases, the SLM provides a programmable spatial weighting function that maps the spatially distributed sample response onto a sequence of single-pixel temporal measurements. The difference between the two layouts mainly arises from practical optical-path constraints and signal-to-noise considerations in the reflection-mode THz-TDS system.

From the reconstruction point of view, the two configurations can be described by the same linear single-pixel imaging model. For a thin transmissive object with spatial transmittance $T(r, f)$ and the i-th SLM pattern $\Phi_i(r)$, the measured single-pixel signal at frequency f can be written as

$$y_i(f) = \int I_0(\mathbf{r}, f)\Phi_i(\mathbf{r})T(\mathbf{r}, f)d\mathbf{r} + n_i \tag{3}$$

where $I_0(r, f)$ is the incident THz field distribution and n_i represents measurement noise. Under the thin-object and paraxial approximation, or when the object and the SLM are placed in the same or optically conjugate transverse plane, $T(r, f)$ and $\Phi_i(r)$ act as multiplicative spatial functions. Therefore, placing the SLM before or after the transmissive sample leads to the same effective sensing equation, except for system-dependent calibration factors such as illumination nonuniformity, propagation loss, finite beam size, and pixel-response variation.

In reflection mode, the same model applies by replacing the transmissive response $T(r, f)$ with the reflective response $R(r, f)$. The frequency-domain single-pixel signal can be written as

$$y_i(t) = \int I_0(\mathbf{r}, t)\Phi_i(\mathbf{r})R(\mathbf{r}, f)d\mathbf{r} + n_i\,. \tag{4}$$

For time-of-flight depth-resolved reconstruction, the selected temporal-delay response $R(r, t)$ is used instead of $R(r, f)$, giving

$$y_i(t) = \int I_0(\mathbf{r}, t)\Phi_i(\mathbf{r})R(\mathbf{r}, t)d\mathbf{r} + n_i\,. \tag{5}$$

Thus, the SLM implements the same measurement matrix in both transmission and reflection geometries. It sequentially applies spatial masks to convert the transmitted or reflected THz field into a set of Hadamard-coded single-pixel measurements. In frequency-resolved imaging, the reconstructed image is obtained from the Fourier-domain amplitude at a selected frequency. In time-of-flight imaging, the reconstructed image is obtained from the temporal signal at a selected delay. Therefore, the depth-resolved reconstruction relies on time-of-flight information preserved in the THz-TDS waveform, rather than on active phase modulation by the SLM.

In the practical reflection-mode system, however, placing the SLM in the return path after the sample is more favorable than placing it in the incident path before the sample. This configuration allows the reflective sample to be illuminated by an unencoded and less perturbed THz beam, while the reflected spatial field carrying the sample information is subsequently encoded by the SLM before reaching the single-pixel detector. If the SLM were placed before the reflective sample, the incident THz pulse would first pass through the GaAs substrate before interacting with the sample. This would introduce additional insertion loss and could generate parasitic temporal features, including internal reflections within the GaAs substrate and weak multiple-reflection echoes associated with the modulator structure. These artifacts would then be carried into the sample illumination and superimposed on the sample-reflected waveform, reducing the reflected-signal signal-to-noise ratio and complicating time-of-flight analysis.

Therefore, in the reflection-mode experiment, the THz beam first illuminates the sample, and the sample-reflected field is then spatially encoded by the SLM along the return optical path before detection. This arrangement should be regarded as receive-side spatial encoding of the sample-reflected field. It preserves the same single-pixel measurement principle as the transmission geometry while providing cleaner sample illumination, reduced pre-sample propagation artifacts, and more reliable temporal features for reflection-mode depth-resolved THz single-pixel imaging.

Supplementary Note 9. TIR-geometry phase-modulation characterization

In the main single-pixel imaging experiments, the THz-SLM is operated in an in-line transmission geometry and functions as an electrically programmable broadband amplitude encoder. The depth and spectral information in the main text are obtained from the coherent THz-TDS waveform, rather than from active phase modulation by the SLM. Here, we provide an additional characterization to show that the same GaAs Schottky microslit platform can also produce electrically tunable reflected phase response when operated in a conductive-interface total-internal-reflection (CI-TIR) geometry.

The phase modulation mechanism in the TIR geometry is different from the in-line transmission amplitude-modulation geometry used for single-pixel imaging. Under supercritical incidence at a high-index/low-index interface, the reflected THz phase depends on the optical sheet conductivity at the conductive interface. When the GaAs Schottky microslit device is placed on a high-resistivity silicon prism, the THz field forms an evanescent wave near the prism/GaAs interface. The subwavelength metal microslits enhance the local evanescent field in the narrow slit gaps when the THz electric field is polarized perpendicular to the microslits. Applying a reverse bias between the Schottky and Ohmic contacts depletes free carriers near the microslits, thereby changing the interfacial sheet conductivity. As a result, the phase of the reflected THz wave can be electrically tuned in the TIR geometry. This principle is consistent with the conductive-interface TIR model reported previously for GaAs Schottky microslit phase modulation.

In the experiment, the SLM was placed on a high-resistivity silicon prism, as shown in Fig. S13a. Due to the limited size of the silicon prism, not all pixels of the 10 × 10 array could be mapped simultaneously. Therefore, Figs. S13b,c show only the pixels within the effective mapping region rather than the full array.

Figs. S13b and S13c show the peak-to-peak amplitude maps of the reflected THz signal when the mapped pixels were biased at 0 V and 5 V, respectively. The dashed region indicates the effective mapping region used for phase analysis. Four representative positions, P1–P4, were selected from this region. For each position, the reflected time-domain waveforms measured at 0 V and 5 V were Fourier transformed, and the voltage-induced phase difference was calculated as $\Delta\varphi(f)$ = unwrap[$\varphi_{5V}(f) - \varphi_{0V}(f)$], where $\varphi_{0V}(f)$ and $\varphi_{5V}(f)$ are the Fourier-domain phases of the reflected THz signals under 0 V and 5 V reverse bias, respectively.

As shown in Fig. S13d, the four selected positions exhibit voltage-induced phase differences over the measured THz frequency range, indicating that the GaAs Schottky microslit array can generate electrically tunable reflected phase responses when operated in the TIR geometry. This TIR-based phase-modulation configuration may provide a potential route toward electrically controlled THz beam steering and phased-array imaging in future implementations.

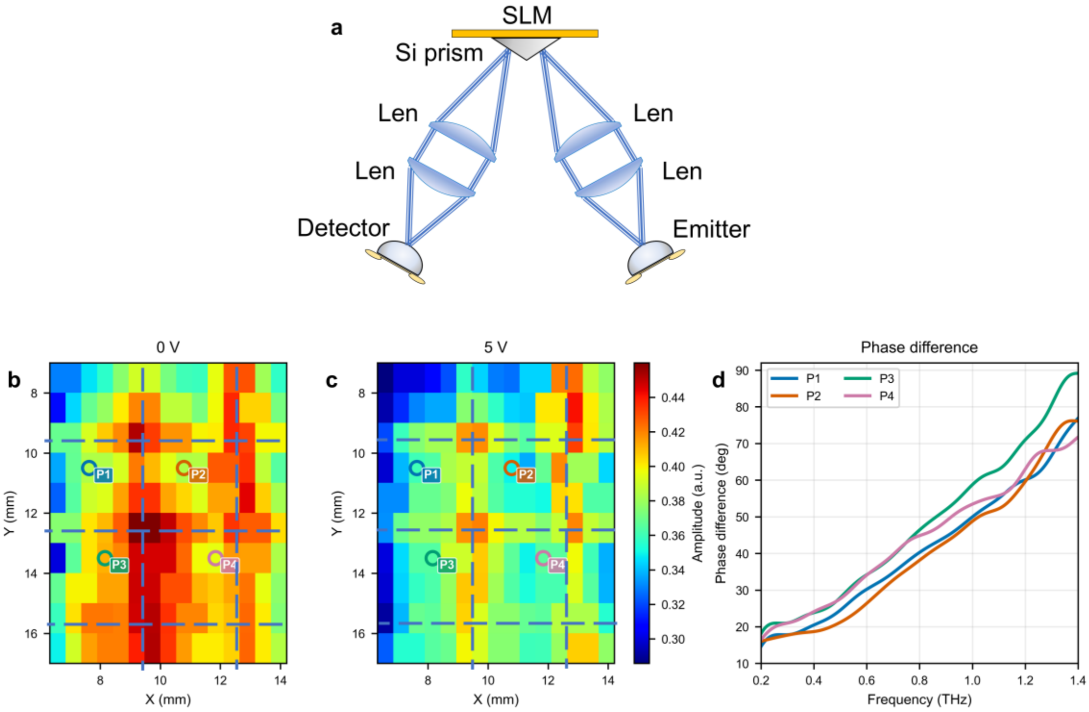

Fig. S13 TIR-geometry phase-modulation characterization of the electrically controlled THz-SLM. a, Schematic of the TIR measurement geometry. The THz-SLM was placed on a high-resistivity silicon prism, and the reflected THz waveform was measured by the THz-TDS system. **b**, **c**, Peak-to-peak amplitude maps of the reflected THz signal when the effective pixels were biased at 0 V and 5 V, respectively. The dashed region indicates the pixel area. Four representative positions, P1-P4, were selected within this region for phase analysis. **d**, Frequency-dependent phase difference between the 5 V and 0 V bias states extracted from the reflected THz-TDS waveforms at P1-P4.

Supplementary Note 10. Current–voltage characterization of a representative GaAs Schottky pixel

To verify the electrical rectifying behavior of the GaAs Schottky microslit structure, the current–voltage (I–V) characteristic was measured from a representative pixel of the THz-SLM array. As shown in Fig. S14, the measured I–V curve exhibits pronounced rectifying behavior, indicating the formation of a Schottky contact in the representative GaAs pixel. Under forward bias, the current increases rapidly with voltage, reaching approximately 69.1 mA at 5 V. Under reverse bias, the current remains negative and relatively small in magnitude, although a non-negligible leakage current is observed at high reverse voltage. The rectification ratio estimated from the currents at ±5 V is approximately 49, indicating clear but moderate Schottky diode behavior. This electrical response supports the voltage-controlled carrier-depletion mechanism used for THz modulation in the GaAs Schottky microslit pixels.

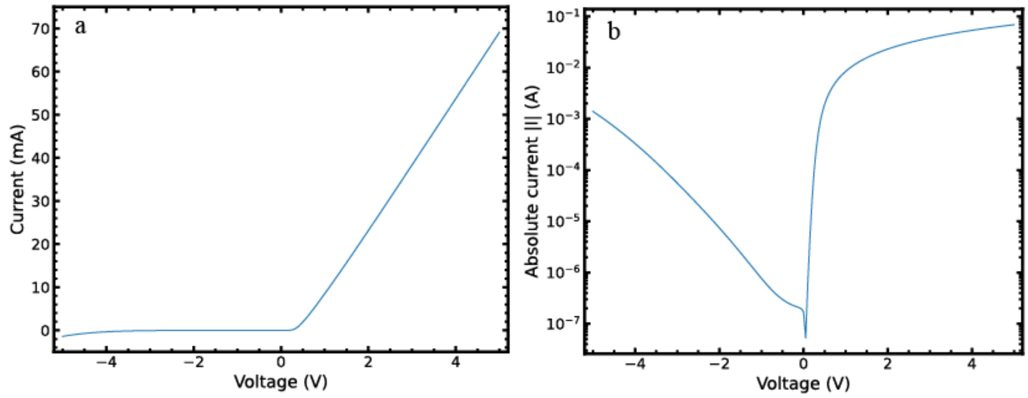

Fig. S14 Current–voltage characteristics of a representative GaAs Schottky pixel. a, Linear-scale I–V curve measured from one selected pixel of the THz-SLM array, showing pronounced rectifying behavior with negative reverse current and rapidly increasing forward current. **b**, Semilogarithmic plot of the absolute current, $|I|$, for the same pixel, highlighting the asymmetric conduction under forward and reverse bias. The current reaches approximately 69.1 mA at +5 V and −1.40 mA at −5 V, corresponding to a rectification ratio of 49 at ±5 V.

Supplementary Note 11. Dynamic THz single-pixel imaging at a fixed temporal delay

For the dynamic experiment, the optical delay line was fixed at a selected temporal position corresponding to a high-amplitude feature of the THz waveform. The detector consequently recorded one fixed-delay field value for each displayed mask rather than a complete time-domain waveform. As illustrated in Fig. S15, the transmitted THz field from the moving target was spatially encoded by the SLM and measured using a mechanical chopper and lock-in amplifier. The chopper provided a stable reference for phase-sensitive detection, while the lock-in amplifier improved the sensitivity and stability of the fixed-delay signal during rapid sequential mask acquisition. The target was translated along the y direction between consecutive acquisitions, and the reconstructed frames show its displacement in the x–y plane.

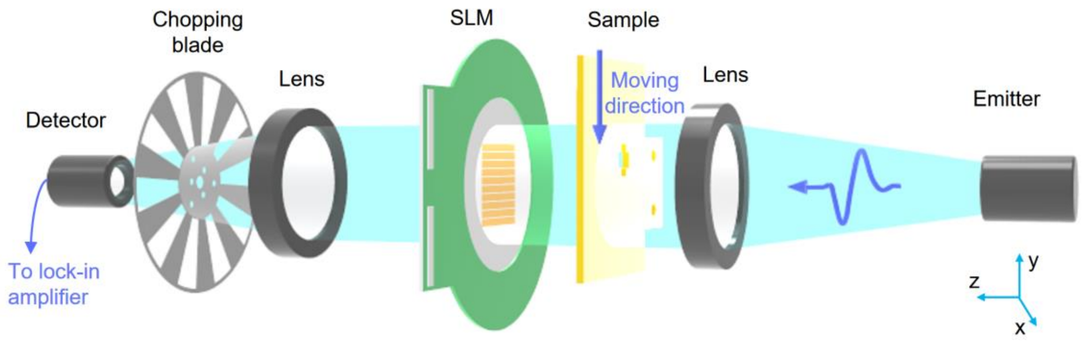

Fig. S15 Experimental configuration for dynamic THz single-pixel imaging. A collimated THz beam illuminates the moving metallic-aperture target, which is translated along the y direction between consecutive image acquisitions. The transmitted field is spatially encoded by the electrically controlled THz-SLM and subsequently detected by a single photoconductive detector. For dynamic imaging, the optical delay line is fixed at a selected temporal position of the THz waveform. A mechanical chopper and lock-in amplifier are used to measure the resulting fixed-delay detector signal with improved sensitivity and stability during sequential mask acquisition.